



**HAL**  
open science

## Accelerated sodium MRI using undersampled 3D SPARKLING at 7T

Renata Porciuncula Baptista, Mathieu Naudin, Chaithya Giliyar  
Radhakrishna, Guillaume Daval-Fr erot, Franck Mauconduit, Alexa Haeger,  
Sandro Romanzetti, Marc Lapert, Philippe Ciuciu, C ecile Rabrait-Lerman, et  
al.

► **To cite this version:**

Renata Porciuncula Baptista, Mathieu Naudin, Chaithya Giliyar Radhakrishna, Guillaume Daval-Fr erot, Franck Mauconduit, et al.. Accelerated sodium MRI using undersampled 3D SPARKLING at 7T. 2023. hal-03929787

**HAL Id: hal-03929787**

**<https://hal.science/hal-03929787>**

Preprint submitted on 9 Jan 2023

**HAL** is a multi-disciplinary open access archive for the deposit and dissemination of scientific research documents, whether they are published or not. The documents may come from teaching and research institutions in France or abroad, or from public or private research centers.

L'archive ouverte pluridisciplinaire **HAL**, est destin ee au d ep ot et  a la diffusion de documents scientifiques de niveau recherche, publi es ou non,  emanant des  tablissements d'enseignement et de recherche fran ais ou  trangers, des laboratoires publics ou priv es.

# 1 Accelerated Sodium MRI using undersampled 3D SPARKLING 2 at 7T

3 Renata Porciuncula Baptista<sup>1,\*</sup>, Mathieu Naudin<sup>2</sup>, Chaithya G R<sup>1,3</sup>, Guillaume  
4 Daval-Fr erot<sup>1,3,4</sup>, Franck Mauconduit<sup>1</sup>, Alexa Haeger<sup>5</sup>, Sandro Romanzetti<sup>5</sup>, Marc Lapert<sup>4</sup>,  
5 Philippe Ciuciu<sup>1,3</sup>, C ecile Rabrait-Lerman<sup>1</sup>, Remy Guillevin<sup>2</sup>, Alexandre Vignaud<sup>1</sup>, Fawzi  
6 Boumezbeur<sup>1</sup>

7 1 NeuroSpin, CEA, CNRS, BAOBAB, University Paris-Saclay, Gif-sur-Yvette, France

8 2 Lab Com I3M, Dactim team LMA CNRS 7348 CHU & University of Poitiers, France

9 3 University Paris-Saclay, CEA, Inria, MIND, Palaiseau , France

10 4 Siemens Healthcare SAS, Saint-Denis, F-93210, France

11 5 Department of Neurology, RWTH Aachen University, Aachen, Germany.

12 \* Corresponding author:

**Name** Fawzi Boumezbeur

**Department** NeuroSpin

**Institute** CEA

13 **Address** Centre d' etudes de Saclay, Building 145,  
F-91191, Gif-sur-Yvette  
France

**E-mail** fawzi.boumezbeur@cea.fr

14 **Manuscript word count:** 3317 out of 5000

**Abstract word count:** 210 out of 250

15 **Detailed Word Count** (not to be included for submission)

16 File: main.tex

17 Sum count: 3525

18 Words in text: 3390

19 Words in headers: 55

20 Words outside text (captions, etc.): 0

21 Number of headers: 22

22 Number of floats/tables/figures: 0

23 Number of math inlines: 50

24 Number of math displayed: 8

25 Subcounts:

26 text+headers+captions (#headers/#floats/#inlines/#displayed)

27 1+0+0 (0/0/0/0) Subsection

28 209+1+0 (1/0/0/0) Abstract

29 747+1+0 (1/0/7/0) Section: Introduction

30 0+3+0 (1/0/0/0) Section: Material and methods

31 265+2+0 (1/0/16/5) Subsection: SPARKLING trajectories

32 160+2+0 (1/0/0/2) Subsection: TPI trajectories

33 383+7+0 (3/0/12/0) Subsection: In vitro experiments

34 212+6+0 (3/0/4/0) Subsection: In vivo experiments

35 306+11+0 (4/0/7/1) Subsection: Data Processing

36 0+1+0 (1/0/0/0) Section: Results

37 50+6+0 (1/0/0/0) Subsection: Expected spatial resolution - Point spread functions

38 85+3+0 (1/0/0/0) Subsection: In vivo  $^{23}\text{Na}$  images

39 238+6+0 (1/0/1/0) Subsection: In vitro validation of TSC quantification

40 63+4+0 (1/0/2/0) Subsection: In vivo TSC maps

41 570+1+0 (1/0/1/0) Section: Discussion

42 101+1+0 (1/0/0/0) Section: Conclusions

43

**Abstract**

**Purpose:** To evaluate the benefits of SPARKLING, a stochastic k-space sampling approach over the deterministic sampling scheme TPI (Twisted Projection Imaging) in the context of accelerated cerebral  $^{23}\text{Na}$  MRI and assessing its impact on tissue sodium concentration (TSC) estimation.

**Methods:** Guided by simulation results, *in vitro* and *in vitro* UTE  $^{23}\text{Na}$  MRI datasets were acquired at a 4 mm isotropic resolution from healthy volunteers using both TPI or SPARKLING trajectories with different acceleration factors (AF) on a 7T MR scanner equipped with a 32 channels head coil. Following reconstruction using NUFFT or Proximal Optimized Gradient Method (POGM) algorithms with or without regularization, respectively, the resulting sodium images were compared in terms of effective resolution (FWHM of the PSF), SNR and overall quality. with an *in vitro* assessment of the accuracy of the TSC was performed via external referencing using a 4-point calibration approach.

**Results:** *In vivo* cerebral sodium images acquired using SPARKLING with an acceleration factor of 32 (TA= 5 min 38 s) are similar to those obtained using TPI at AF=8 (TA= 22 min 34 s) with minimal impact on the accuracy of our TSC quantification.

**Conclusion:** In conditions compatible with clinical examination, undersampled SPARKLING  $^{23}\text{Na}$  MRI can outperform the conventional TPI k-space sampling scheme allowing for shorter acquisition times.

**Keywords:**  $^{23}\text{Na}$ , SPARKLING, UHF, human brain, TSC, compressed sensing

## 64 Introduction

65 Cerebral sodium ( $^{23}\text{Na}$ ) magnetic resonance imaging (MRI) provides unique information about brain  
66 tissue viability *in vivo*. Indeed, neurons rely on the energy-hungry sodium-potassium ( $\text{Na}^+/\text{K}^+$ -  
67 ATPase) pump to regulate their transmembrane  $\text{Na}^+$  and  $\text{K}^+$  concentration gradients, which in their  
68 turn define their resting membrane potential. In pathological conditions where the cell membranes  
69 are damaged or their energy synthesis capabilities are compromised, an increase in intracellular  
70 sodium concentration is bound to occur, while extracellular sodium concentration stays constant.  
71 This leads to an increase in tissue sodium concentration (TSC), neuronal dysfunction, and ultimately  
72 cell death (Mccarthy et al., 2015).

73 Therefore changes in TSC are considered potential early biomarkers for many neurodegenerative  
74 diseases. Several studies confirmed the relevance of assessing tissue sodium concentration (TSC) in  
75 neurological disorders such as Alzheimer’s (Haeger et al., 2021), Multiple Sclerosis (MS) (Zaaraoui  
76 et al., 2012; Eisele et al., 2019), Huntington’s, (Reetz et al., 2012) and others (Zaric et al., 2021).

77 However,  $^{23}\text{Na}$ -MRI faces several technical challenges, limiting its clinical use. This is mainly due  
78 to the moderate sodium concentration in the human brain (about 40 mM in the brain parenchyma  
79 and 140 mM in the cerebrospinal fluid (CSF)) and its low intrinsic nuclear magnetic resonance  
80 (NMR) sensitivity compared to proton MRI. In the healthy brain, those differences can lead to up  
81 5500 fold less Signal-To-Noise Ratio (SNR) (Ladd et al., 2018) . Consequently,  $^{23}\text{Na}$  images have  
82 to be acquired at lower spatial resolutions and require long acquisition time (TA) compared to  $^1\text{H}$   
83 MRI..

84 Another difficulty is the fast transverse relaxation times ( $T_2/T_2^*$ ) of  $^{23}\text{Na}$  NMR signal, which are  
85 typically less than 5 ms (Ridley et al., 2018). Consequently, ultra-short echo time (UTE) sequences  
86 combined with deterministic non-Cartesian k-space trajectories have been preferred (Konstandin  
87 and Nagel, 2014) by the  $^{23}\text{Na}$  MRI community. Among the most commonly used non-Cartesian  
88 k-space sampling schemes, we can cite radial, density-adapted three-dimensional radial projection  
89 reconstruction pulse sequence (DA-3DPR) (Nagel et al., 2009), twisted projection imaging (TPI)  
90 (Boada et al., 1997) or Fermat-looped orthogonally-encoded trajectories (FLORET) (Robison et al.,  
91 2017).

92 These standard non-Cartesian readouts are flexible, as they are analytically and geometrically  
93 constrained, and, when combined with density-compensated reconstruction, can provide good image  
94 quality. However they can be sub-optimal in sampling the k-space, especially for  $\mathbf{k}$  values at the

95 borders of  $\mathbf{k}$ -space which can lead to fast degrading spatial resolutions when the  $\mathbf{k}$ -space is under-  
96 sampled (as demonstrated by their computed point spread function (PSF) (Konstandin and Nagel,  
97 2014)). In recent years, compressed-sensing (CS) approaches have been proposed for proton MRI  
98 (Dale et al., 2004; Mir et al., 2004; Kumar Anand et al., 2008; Vasanawala et al., 2010) in order to  
99 to accelerate image acquisition while preserving image quality.

100 At first, proton MRI CS approaches took advantage (i) of the sparse characteristic of MRI signals,  
101 (ii) incoherent sampling schemes, and (iii) nonlinear reconstruction with a sparsity promoting prior.  
102 Currently, the concept of an incoherent sampling scheme is considered sub-optimal (Adcock et al.,  
103 2017) and newer CS techniques focus on (i) globally variable density sampling non-uniformly the  
104 high and low spatial frequencies but managing (ii) a locally uniform coverage of  $\mathbf{k}$ -space (Donoho,  
105 2006).

106 Recently, Chen et al. reviewed the first attempts at applying CS to  $^{23}\text{Na}$  MRI (Chen et al., 2021).  
107 Some of those studies have evaluated the impact of acceleration on TSC, as TSC is the primary goal  
108 of  $^{23}\text{Na}$  MRI. Twelve out of seventeen studies used radial or DA-3DPR as a sampling scheme, and  
109 only one used a version of TPI (Nagel et al., 2009). Yet the authors assumed the incoherence of those  
110 density-adapted three-dimensional radial projection reconstruction pulse sequence (DA-3DPR) or  
111 TPI trajectories. Indeed, the efficacy of CS approach relies on the fulfilment of an "incoherence"  
112 criterion. This criterion states that the measurement basis and the sparse representation basis must  
113 be uncorrelated so that the  $\mathbf{k}$ -space undersampling artifacts add incoherently to the sparse signal  
114 coefficients. While few studies have proposed optimized undersampling schemes for proton MRI by  
115 using a series of second-order cone optimization sub-problems, ideas from the missile guidance field  
116 or other strategies (Kumar Anand et al., 2008; Mir et al., 2004; Dale et al., 2004), none of those  
117 previously cited CS  $^{23}\text{Na}$  MRI studies explored such solutions to optimize the incoherence of their  
118 undersampled density-adapted three-dimensional radial projection reconstruction pulse sequence  
119 (DA-3DPR) or TPI trajectories.

120 Here, we propose to apply SPARKLING (Spreading Projection Algorithm for Rapid  $\mathbf{K}$ -space  
121 sampLING) (Lazarus et al., 2020; Chaithya et al., 2022) to accelerate  $^{23}\text{Na}$  MRI acquisitions.  
122 SPARKLING is inspired by CS approaches with a (i) global variable density sampling but (ii)  
123 locally uniform coverage of  $\mathbf{k}$ -space. Compared to more classical approaches, this approach is an  
124 excellent candidate for shortening the TA while preserving image quality in  $^{23}\text{Na}$  MRI.

125 The application of CS techniques to sodium imaging presents its specific challenges because the  
126 acceleration achievable using CS approaches depends on the image size and available SNR: for both,

127 the bigger it is, the better Lazarus et al. (2018). Unfortunately for  $^{23}\text{Na}$  MRI, both are limiting  
 128 factors compared to  $^1\text{H}$  MRI.

129 In this study, for the first time, we aimed at demonstrating that we can accelerate *in vivo*  
 130  $^{23}\text{Na}$  acquisitions at 7T and perform valid TSC quantification using 3D SPARKLING. We compare  
 131 our effort to current state-of-the-art TPI acquisitions with identical acquisitions parameters ( $T_{obs}$ ,  
 132 bandwidth (BW), flip angle, and repetition time (TR)). Our study design was divided in two parts  
 133 (i) *in vitro* measurements to assess the impact of the different AF on TSC quantification, and (ii) *in*  
 134 *vivo* experiments to analyze the resulting quality of our cerebral TSC maps acquired from healthy  
 135 human volunteers.

## 136 Material and methods

### 137 SPARKLING trajectories

138 The SPARKLING algorithm (Lazarus, 2019) generates optimized k-space sampling patterns  $\mathbf{K}[i] =$   
 139  $(k_{x,i}, k_{y,i}, k_{z,i})$ , where  $i$  represents a sample which comply to a target acquisition density. At the  
 140 same time, SPARKLING respects MR hardware limitations such as maximum gradient amplitudes  
 141 and slew rates. SPARKLING generally focuses on radially symmetric densities, which present the  
 142 advantage of yielding results invariant to translation and rotation of the sample to the image. This  
 143 target density is defined by two parameters: cutoff (C) and decay (D) (figure 1). They are defined  
 144 as follows:

$$\pi_{C,D}(x) = \begin{cases} K & |x| < C \\ K \left(\frac{C}{|x|}\right)^D & |x| > C \end{cases} \quad [1]$$

where  $K$  is a constant obtained through normalization:

$$K = \frac{1 - D}{2C(C^{D-1} - D)}$$

145 This algorithm has been extended to 3D and is described in detail elsewhere (Chaithya et al.,  
 146 2022). 3D SPARKLING offers a locally uniform coverage of k-space, differently from TPI or radial  
 147 strategies. The trajectory  $\hat{\mathbf{K}}$  is optimized as:

$$\hat{\mathbf{K}} = \arg \min_{\mathbf{K}} F_p(\mathbf{K}) = F_p^a(\mathbf{K}) - F_p^r(\mathbf{K}) \quad [2]$$

148 where  $F_p^a(\mathbf{K})$  is the attraction term enforcing the sampling pattern  $\mathbf{K}$  and  $F_p^r(\mathbf{K})$  is the repulsion  
 149 term which guarantees a good filling of the k-space. The repulsion term  $F_p^r(\mathbf{K})$  and  $F_p^a(\mathbf{K})$  are  
 150 defined as:

$$F_p^r(\mathbf{K}) = \frac{1}{2p^2} \sum \|\mathbf{K}[i] - \mathbf{K}[j]\|_2 \quad [3a]$$

$$F_p^a(\mathbf{K}) = \frac{1}{p} \sum \int_{\omega} \|(x - \mathbf{K}[i])\|_2 \rho(x) dx \quad [3b]$$

151 Here, we adopted a variation of SPARKLING, called MORE SPARKLING, (Chaithya G R  
 152 et al., 2022) to define sets of center-out spokes for  $^{23}\text{Na}$  imaging. In this variation, the  $F_p^r$  factor  
 153 incorporates a temporal weighting that notably enforces spokes to homogeneously move away from  
 154 the center and is defined as:

$$F_p^r(\mathbf{K}) = \frac{1}{2p^2} \sum \exp^{|t_i - t_j|} \|\mathbf{K}[i] - \mathbf{K}[j]\|_2 \quad [4a]$$

155 where  $t_i$  and  $t_j$  correspond to the times when the samples  $\mathbf{K}[i]$  and  $\mathbf{K}[j]$  are acquired. This is  
 156 important to reduce off-resonance artifacts and avoid signal loss due to averaging points at different  
 157 observation times, which is especially important for the fast relaxing sodium nuclei.

158 The calculation of  $F_p^r$  and  $F_p^a$  is made through a gradient descent algorithm (Chaithya et al.,  
 159 2022). The code has been optimized for GPU computing, (Chaithya et al., 2022). Interested  
 160 researchers are invited to contact the authors to obtain access to this package.

## 161 TPI trajectories

162 Twisted projection trajectories (TPI) were introduced in 1997 (Boada et al., 1997). At that time,  
 163 the state-of-the-art k-space sampling schemes for  $^{23}\text{Na}$  MRI were based on radial trajectories. The  
 164 premise behind TPI is that improvements in the sampling efficiency of three dimensional projection  
 165 imaging can be attained by removing the non-uniform sample density that results from uniform  
 166 sampling in time along radial lines in k-space.

167 In three dimensions, the improvement in the efficiency is done through a twist in the trajectories  
 168 that preserves the sample density. In a thin spherical shell the number of trajectories will be constant  
 169 if the number of samples inside a thin spherical shell is proportional to the volume of the shell. This  
 170 can be describe through the equations:

$$\dot{k} = \frac{\alpha}{k^2} \quad [5]$$

and

$$\dot{k} + k^2(\dot{\theta} + \sin^2 \theta \dot{\varphi}^2) = \gamma^2 G^2 \quad [6]$$

171 Examples of TPI and SPARKLING trajectories can be seen in figure 2. The algorithm to gen-  
 172 erate TPI trajectories was implemented in MATLAB along with others (radial and density adaptive  
 173 radial) and they are available in a public repository (<https://github.com/rpbaptista/Trajectories/>).

## 174 **In vitro experiments**

### 175 **Test objects**

176 For our in vitro acquisitions, a realistic human head phantom was used Jona et al. (2021). This  
 177 phantom is composed of two compartments (figure 3): the inner compartment was filled with a  
 178 solution of 40 mmol/L of NaCl and the outer compartment was filled with a NaCl solution at a  
 179 higher concentration of 100 mmol/L. This phantom with known design and concentrations was used  
 180 to assess the effect of the different acceleration strategies on TSC quantification.

181 For TSC calibration, four cylindrical 50mL tubes were filled with 2% agarose gels to obtain  
 182 shorter, more realistic relaxation times for  $^{23}\text{Na}$ . Sodium (NaCl) concentrations for each tubes were:  
 183 51, 105, 155 and 209 mM. For each acquisition and reconstruction, the tubes were masked and the  
 184 signal intensity histograms were analyzed to estimate the reference signal value corresponding to  
 185 each known sodium concentrations by considering the  $N^{\text{th}}$  percentile of the signal distribution, the  
 186 precise value of this percentile (ranging from 50 to 70) was calibrated separately from full Nyquist  
 187 images to account for the different partial-volume effects and artifacts affecting the signal intensity  
 188 distributions in the reference tubes.

### 189 **Data acquisition**

190  $^{23}\text{Na}$  MRI sequence parameters were those determined previously by Coste et al. (2019) to maximize  
 191 SNR for *in vivo*  $^{23}\text{Na}$  MRI: TE/TR=0.8/20 ms, FOV=296 mm isotropic, FA= 55°, gradient raster  
 192 time = 10  $\mu\text{s}$ , dwell time = 2  $\mu\text{s}$ ,  $T_{obs}$  = 12.48 ms,  $N_s$ =6240, 32 averages, oversampling factor (OS)  
 193 was set to 5.

194 As a reference image, a 3D radial acquisition fulfilling the Nyquist criteria ( $N_s \geq 4\pi(k_{max}FOV)^2$ )  
 195 was performed. The acceleration factor (AF) was defined relatively to this full-Nyquist radial ac-  
 196 quisition:  $\left( AF = \frac{N_{s_{radialfullNyquist}}}{N_{s_{currentacquisition}}} \right)$ .

197 For TPI acquisitions, the radial fraction parameter was set at 0.3, it was optimal parameter  
 198 in the literature Romanzetti et al. (2014). For SPARKLING acquisitions, the cutoff and decay  
 199 parameters of the targeted density function were:  $C = 30\%$  and  $D = 2$  (Fig 2). Four different  
 200 acceleration factors (AF=(8,32,64,128), TA=(22°30',5'40",2'48",1'28")) were explored for both TPI  
 201 and SPARKLING sampling schemes. (Fig 2).

202  $^{23}\text{Na}$  images were acquired at two flip angles ( $VFA_1=25^\circ/VFA_2 = 50$ ) to allow for TSC quan-  
 203 tification according to our Variable Flip Angle (VFA) approach Coste et al. (2019).

204 The  $B_1^+$  field map was measured with the TPI sequence using a double angle method (DAM)  
 205 (Stollberger and Wach, 1995) approach with  $\alpha_1/\alpha_2 = 45/90$  at 8 mm isotropic and TE/TR=0.8/120  
 206 ms. The acquisition time was 1 min 36 seconds per scan. The  $B_1^+$  map was used to improve the  
 207 robustness of the computed  $T_1$  and  $M_0$  maps.

## 208 In vivo experiments

### 209 Participants

210 This study was approved by local and French national ethics committees (2019-A02689-48) informed  
 211 consent was obtained from all participants. Five healthy volunteers were recruited. The participants  
 212 were split in two groups: one cohort in which image quality was assessed (1M/1F) ( $35 \pm 5$  years old)  
 213 and a second cohort (2M/1F) ( $22 \pm 6$  years old) in which the accuracy of the TSC quantification  
 214 was assessed.

### 215 Data acquisition

216 MRI data were acquired on a Terra 7T MRI scanner (Siemens Healthineers, Erlangen, Germany)  
 217 equipped with a whole-body gradient coil ( $G_{max}=80\text{mT/m}$ , slew rate of  $200\text{mT/m/s}$ ) and a double-  
 218 tune 1Tx/1Rx birdcage coil for  $^1\text{H}$  and 1Tx/32Rx helmet coil for  $^{23}\text{Na}$  (Rapid Biomedical GmbH,  
 219 Rimpfing, Germany).

220 In vivo acquisitions also included an  $T_1$ -weighted image (MPRAGE, TE/TR/TI = 1.85/1310/500  
 221 ms, FA=  $6^\circ$ , 1 mm isotropic resolution, TA=3:46 min) for anatomical reference. An iterative second-  
 222 order  $B_0$  shimming procedure was performed and the optimal shimming parameters were used during

223 the sodium acquisitions.

224 Sequence parameters for our  $^{23}\text{Na}$  MRI and  $B_1^+$  field acquisitions were identical to our in vitro  
225 acquisitions.

226 For the three volunteers of the second cohort, and only for AF=32, 64 and 128 (due to the  
227 limited examination time),  $^{23}\text{Na}$  images were acquired using the second flip angle of  $25^\circ$  to allow for  
228 TSC quantification Coste et al. (2019).

## 229 Data Processing

### 230 Image reconstruction

231 Density compensation (Pipe and Menon, 1999) was performed using Pysap-MRI (El Gueddari  
232 et al., 2020) in all the data. This package allows for the management of large 3D non-Cartesian  
233 multichannel datasets. The iterative method was the same for TPI and SPARKLING datasets.  
234 As the density compensation function depends solely on the k-space trajectories, the comparison  
235 between TPI and SPARKLING acquisitions remains fair.

236 While iterative reconstruction methods are expected to be used for CS acquisitions since they  
237 typically yield nicer images, it would be difficult to discriminate between the benefits of the un-  
238 dersampled trajectories and those of the iterative reconstruction. Consequently, we chose to re-  
239 construct and evaluate our data using both an iterative reconstruction method using proximal  
240 optimized gradient method (POGM) (Kim et al., 2021) and an non-iterative regridding method  
241 using NUFFT (Fessler and Sutton, 2003).

242 Our non-linear iterative reconstruction can be described as follows:

$$\hat{\mathbf{z}} = \arg \min_{\mathbf{z}} \frac{1}{2} \|\mathbf{y} - \mathbf{z}\|_2^2 + \lambda \|\mathbf{z}\|_1$$

243 For each iterative reconstruction, the regularization parameter ( $\lambda$ ) were selected visually in the  
244  $10^{-7}$  to  $10^{-20}$  range (30 steps) to maximize image quality.  $\lambda$  was kept constant between volunteers  
245 for a given acceleration factor and a given trajectory.

### 246 TSC Quantification

247 In this study, the variable flip angle (VFA) approach was used as described in Coste et al. (2019)  
248 to estimate  $M_0$  maps which were corrected for residual  $T_1$ -weighting from the combination of two  
249 sodium images acquired at two different FA. Those  $M_0$  images were also corrected for any  $B_1^+$

250 inhomogeneities by accounting for the effective flip angles as measured from the independently  
251 acquired  $B_1^+$  field map.

252 To obtain quantitative TSC maps, four 50mL tubes were used as external references of con-  
253 centration. The quantification process consisted in automatically segmenting those tubes in the  
254  $^{23}\text{Na}$  images, extracting their signal intensity distribution and performing a four-point linear re-  
255 gression using the reference signal values corresponding to each tubes against their known sodium  
256 concentrations.

### 257 **Evaluation of TSC quantification accuracy**

258 The accuracy of the TSC quantification was evaluated based on in vitro  $^{23}\text{Na}$  images of the an-  
259 thropomorphic human head phantom with known sodium concentrations. Relative errors in the  
260 TSC quantification were calculated and compared between undersampled TPI and SPARKLING  
261 acquisitions.

## 262 **Results**

### 263 **Expected spatial resolution - Point spread functions**

264 Table 1 summarizes the FWHM of the PSF computed for each set of SPARKLING and TPI spokes.  
265 The effective spatial resolution was consistently higher for undersampled SPARKLING trajectories  
266 compared to their TPI counterparts. Figure 4 shows the central slice of the log of the PSF for the  
267 investigated TPI and SPARKLING trajectories.

### 268 **In vivo $^{23}\text{Na}$ images**

269 Figure 5 shows a gallery of axial  $^{23}\text{Na}$  MRI obtained from our first two healthy volunteers. As  
270 expected from the comparison of the PSF, undersampled SPARKLING strategies seems to better  
271 preserve high spatial frequency details such as the cortex delineation for bigger accelerations factors  
272 compared to TPI. This is particularly clear when comparing the images acquired with SPARKLING  
273 with an  $\text{AF}=32$  to the ones acquired with TPI and an  $\text{AF}=8$ .

274 Figure 6 shows the result of the reconstruction of our accelerated  $^{23}\text{Na}$  MRI using the POGM  
275 algorithm.

## 276 **In vitro validation of TSC quantification**

277 For all our linear regressions performed across different accelerations factors for calibration,  $R^2$   
278 values were systematically superior to 0.96, demonstrating the robustness of the 4-point calibration  
279 method (see figure S1 for illustration).

280 Tables 2 and 3 summarize the average sodium concentration in the inner compartment of our  
281 anthropomorphic phantom estimated from TSC maps acquired *in vitro* with the different under-  
282 sampled strategies and reconstructed with NUFFT or POGM respectively.

283 One can notice that undersampled TPI acquisitions lead to slightly larger apparent sodium  
284 concentration and quantification errors compared to undersampled SPARKLING acquisitions. This  
285 is consistent with the broader PSF of undersampled TPI. Yet for both TPI and SPARKLING, the  
286 quantification remained quite accurate up to an acceleration factor of 32, the relative quantification  
287 error being at about 2.5% when NUFFT was used for the reconstruction.

288 When using the POGM iterative method, the resulting TSC maps exhibited systematically  
289 larger quantification errors than their NUFFT counterparts. Yet for AF=8 or even for AF=32 and  
290 SPARKLING, the quantification bias introduced by the regularization in POGM seemed to be  
291 manageable.

292 For both trajectories, the higher accelerations were extremely detrimental to the accuracy of  
293 the quantification and should not be considered as a viable option for quantitative  $^{23}\text{Na}$  MRI. For  
294 instance, for AF=128, the resulting TSC maps displayed relative errors of about 85% for TPI and  
295 67.5% for SPARKLING with the NUFFT reconstruction. These values would increase to 175% for  
296 TPI and 153% for SPARKLING when POGM is used.

## 297 **In vivo TSC maps**

298 Figure 7 shows the TSC maps acquired from three healthy volunteers using both TPI and SPARKLING  
299 trajectories with an acceleration factor of 32 (acquisition time = 5'40"). As already observed for  
300 our *in vitro* data, TSC values were found sensibly higher for TPI compared to SPARKLING, the  
301 average difference being  $2 \pm 3$  mM when using the NUFFT reconstruction whereas it was  $11 \pm 2$   
302 mM when using the iterative POGM iterative reconstruction.

## Discussion

In this study, we investigated for the first time the application of SPARKLING (precisely MORE-SPARKLING) Lazarus (2019); Chaithya G R et al. (2022), a stochastic k-space sampling strategy to accelerate the acquisition of quantitative  $^{23}\text{Na}$  MRI of the human brain at 7T.

As a popular and efficient deterministic non-Cartesian k-space sampling scheme, undersampled TPI datasets Boada et al. (1997) were acquired systematically to serve as comparison points.

From those comparisons, one can conclude that in the right conditions (i.e. at 7T for a resolution of 4 mm isotropic, a 32 channel coil and 32 averages) undersampled SPARKLING acquisitions outperform TPI for the same AF both in terms of image quality and accuracy of the TSC quantification.

In particular, we observed that sodium images acquired using undersampled SPARKLING at AF=32 exhibited similar visual qualities than the ones acquired using undersampled TPI at AF=8. We also estimated that this level of acceleration (AF=32) using SPARKLING (with either NUFT or POGM reconstructions) led to acceptable quantification errors (2,5%) while the relative error for TPI and AF=32 was much larger (27%).

There are likely two reasons for these differences between undersampled TPI and SPARKLING strategies. The first one should be the narrower PSF estimated for SPARKLING compared to TPI for the same number of spokes (Table 1). It is of import to notice than these computed PSF did not take into account the impact of  $B_0$  inhomogeneities across the brain, nor the influence of the reconstruction algorithm used of CS reconstructions. Such evaluation is not trivial and was not explored in this work. The second factor should be that deterministic trajectories such TPI are less likely to satisfy the "incoherence criterion" compared to the stochastic SPARKLING approach, especially in absence of some optimization of the undersampling of k-space.

Recent studies (Gnahm et al., 2014; Blunck et al., 2020) have explored CS techniques for 3 mm isotropic at 7T while using DA-3DPR. Here, we targeted a resolution of 4 mm isotropic, which is a good trade-off for clinical examination in terms of TA and image quality. The authorship should refrain from extrapolating these results to different spatial resolutions or nuclei as the performance of CS approaches depends strongly on the available SNR and image sizes. This means that deterministic k-space sampling strategies such as TPI remain of actuality in most scenarios, especially in absence of acceleration or for modest acceleration factors.

As the determination of scenarios of interest for SPARKLING is not trivial (Lazarus, 2019), a

334 simulation tool was developed to assess efficiently different scenarios in silico (Porciuncula Baptista  
335 et al., 2022).

336 In preliminary studies, we measured image quality via the structural similarity index measure  
337 (SSIM) compared to a Full-Nyquist radial reference. This approach was not kept because SSIM  
338 (Wang et al., 2015) is known to not be robust to blurring effects and PSF distortions, leading to  
339 misleading results, ie, high SSIM and low image quality.

340 One of the main limitation of SPARKLING as a k-space sampling strategy is its lack of flex-  
341 ibility. Indeed, compared to deterministic and parametric sampling schemes, the computation of  
342 SPARKLING trajectories is quite intensive and the different trajectories must be determined of-  
343 fline or made available in a library. These constitute real hurdles for the future application of such  
344 approach in a clinical research setting. Still we believe that improvements in image quality and  
345 reduction in acquisition times while preserving the accuracy of the TSC quantification are worth  
346 the continuing investment in developing and implementing ever faster optimization techniques and  
347 reconstruction systems.

348 In the future, those promising results could be improved further by adding a priori anatomical  
349 constraints or using dictionary learning techniques (Behl et al., 2016).

## 350 Conclusions

351 For the first time, SPARKLING a novel k-space sampling strategy for CS MRI was applied success-  
352 fully to accelerate the acquisition of  $^{23}\text{Na}$  MRI at 7T in few healthy volunteers. We showed that  
353 in those favorable conditions, the acquisition of quantitative TSC maps could be accelerated by a  
354 factor 32 using SPARKLING with minimal loss of anatomical details or accuracy in the calibration  
355 process. Besides the application of those accelerated TSC maps to investigate abnormally high TSC  
356 values in brain pathologies, the relative rapidity of these  $^{23}\text{Na}$  acquisitions could be of interest to  
357 revisit the sodium changes observed during neuronal activation as proposed by Bydder et al. (2019).

## 358 Acknowledgments

359 This work received financial support from Leducq Foundation (large equipment ERPT program,  
360 NEUROVASC7T project). Chaithya G R was supported by the CEA NUMERICS program, which  
361 has received funding from the European Union’s Horizon 2020 research and innovation program

362 under the Marie Skłodowska-Curie grant agreement No 800945. This work was granted access to  
363 the HPC resources of IDRIS under the allocation 2021-AD011011153 made by GENCI.

## 364 References

365 Adcock B, Hansen AC, Poon C, Roman B. 2017. Breaking the coherence barrier: A new theory for  
366 compressed sensing. *Forum of Mathematics, Sigma* 5. doi:10.1017/fms.2016.32. 1302.0561.

367 Behl NG, Gnahn C, Bacher T P, Ladd ME, Nagel AM. 2016. Three-dimensional dictionary-learning  
368 reconstruction of  $^{23}\text{Na}$  MRI data. *Magnetic Resonance in Medicine* 75:1605–1616. doi:10.1002/  
369 mrm.25759.

370 Blunck Y, Kolbe SC, Moffat BA, Ordidge RJ, Cleary JO, Johnston LA. 2020. Compressed sensing  
371 effects on quantitative analysis of undersampled human brain sodium MRI. *Magnetic Resonance*  
372 *in Medicine* 83:1025–1033. doi:10.1002/mrm.27993.

373 Boada FE, Gillen JS, Shen GX, Chang SY, Thulborn KR. 1997. Fast three dimensional sodium  
374 imaging. *Magnetic Resonance in Medicine* 37:706–715. doi:10.1002/mrm.1910370512.

375 Bydder M, Zaaraoui W, Ridley B, Soubrier M, Bertinetti M, Confort-Gouny S, Schad L, Guye M,  
376 Ranjeva JP. 2019. Dynamic  $^{23}\text{Na}$  MRI - A non-invasive window on neuroglial-vascular mecha-  
377 nisms underlying brain function. *NeuroImage* 184:771–780. doi:10.1016/j.neuroimage.2018.09.071.

378 Chaithya G, Weiss P, Daval-Fr erot G, Massire A, Vignaud A, Ciuciu P. 2022. Optimizing full  
379 3d sparkling trajectories for high-resolution magnetic resonance imaging. *IEEE Transactions on*  
380 *Medical Imaging* :1–1doi:10.1109/TMI.2022.3157269.

381 Chaithya G R, Guillaume Daval-Fr erot, Aur elien Massire, Boris Mailhe, Mariappan Naddar, Alexan-  
382 dre Vignaud, Philippe Ciuciu. 2022. MORE-SPARKLING: Non-Cartesian trajectories with Min-  
383 imized Off-Resonance Effects. In: *Proceedings of the 30th International Society of Magnetic*  
384 *Resonance in Medicine*.

385 Chen Q, Shah NJ, Worthoff WA. 2021. Compressed Sensing in Sodium Magnetic Resonance Imaging:  
386 Techniques, Applications, and Future Prospects. *Journal of Magnetic Resonance Imaging* :1–  
387 17doi:10.1002/jmri.28029.

- 388 Coste A, Boumezbeur F, Vignaud A, Madelin G, Reetz K, Le Bihan D, Rabrait-Lerman C, Ro-  
389 manzetti S. 2019. Tissue sodium concentration and sodium T1 mapping of the human brain  
390 at 3 T using a Variable Flip Angle method. *Magnetic Resonance Imaging* 58:116–124. doi:  
391 10.1016/j.mri.2019.01.015.
- 392 Dale BM, Lewin JS, Duerk JL. 2004. Optimal design of k-space trajectories using a multi-objective  
393 genetic algorithm. *Magnetic Resonance in Medicine* 52:831–841. doi:10.1002/mrm.20233.
- 394 Donoho DL. 2006. Compressed sensing. *IEEE Transactions on Information Theory* 52:1289–1306.  
395 doi:10.1109/TIT.2006.871582.
- 396 Eisele P, Konstandin S, Szabo K, Ebert A, Roßmanith C, Paschke N, Kerschensteiner M, Platten  
397 M, Schoenberg SO, Schad LR, Gass A. 2019. Temporal evolution of acute multiple sclerosis  
398 lesions on serial sodium ( $^{23}\text{Na}$ ) MRI. *Multiple Sclerosis and Related Disorders* 29:48–54. doi:  
399 10.1016/j.msard.2019.01.027.
- 400 El Gueddari L, Gr C, Ramzi Z, Farrens S, Starck S, . 2020. PySAP-MRI: a Python Package for  
401 MR Image Reconstruction. . . . *Image Reconstruction* :8.
- 402 Fessler J, Sutton B. 2003. Nonuniform fast fourier transforms using min-max interpolation. *IEEE*  
403 *Transactions on Signal Processing* 51:560–574. doi:10.1109/TSP.2002.807005.
- 404 Gnahn C, Bock M, Bachert P, Semmler W, Behl NG, Nagel AM. 2014. Iterative 3D projec-  
405 tion reconstruction of  $^{23}\text{Na}$  data with an  $^1\text{H}$  MRI constraint. *Magnetic Resonance in Medicine*  
406 71:1720–1732. doi:10.1002/mrm.24827.
- 407 Haeger A, Bottlaender M, Lagarde J, Porciuncula Baptista R, Rabrait-Lerman C, Luecken V,  
408 Schulz JB, Vignaud A, Sarazin M, Reetz K, Romanzetti S, Boumezbeur F. 2021. What can 7T  
409 sodium MRI tell us about cellular energy depletion and neurotransmission in Alzheimer’s disease?  
410 *Alzheimer’s and Dementia* 17:1843–1854. doi:10.1002/alz.12501.
- 411 Jona G, FurmanHaran E, Schmidt R. 2021. Realistic head[U+2010]shaped phantom with  
412 brain[U+2010]mimicking metabolites for 7 T spectroscopy and spectroscopic imaging. *NMR*  
413 *in Biomedicine* 34. doi:10.1002/nbm.4421.
- 414 Kim SY, Song J, Yoon JH, Kim KN, Chung JY, Noh Y. 2021. Voxel-wise partial volume correction  
415 method for accurate estimation of tissue sodium concentration in  $^{23}\text{Na}$ -MRI at 7 T. *NMR in*  
416 *Biomedicine* 34:3–5. doi:10.1002/nbm.4448.

- 417 Konstandin S, Nagel AM. 2014. Measurement techniques for magnetic resonance imaging of fast  
418 relaxing nuclei. *Magnetic Resonance Materials in Physics, Biology and Medicine* 27:5–19. doi:  
419 10.1007/s10334-013-0394-3.
- 420 Kumar Anand C, Thomas Curtis A, Kumar R. 2008. Durga: A heuristically-optimized data collec-  
421 tion strategy for volumetric magnetic resonance imaging. *Engineering Optimization* 40:117–136.  
422 doi:10.1080/03052150701641783.
- 423 Ladd ME, Bachert P, Meyerspeer M, Moser E, Nagel AM, Norris DG, Schmitter S, Speck O, Straub  
424 S, Zaiss M. 2018. Pros and cons of ultra-high-field mri/mrs for human application. *Progress in*  
425 *Nuclear Magnetic Resonance Spectroscopy* 109:1–50. doi:https://doi.org/10.1016/j.pnmrs.2018.  
426 06.001.
- 427 Lazarus C. 2019. Compressed Sensing in MRI : optimization-based design of k-space filling curves  
428 for accelerated MRI To cite this version : L ' echantillonnage compressif en IRM : conception  
429 optimis ee trajectoires d ' echantillonnage ´ erer pour acc el l ' IRM. [[Doctoral thesis]]: .
- 430 Lazarus C, Weiss P, El Gueddari L, Mauconduit F, Massire A, Ripart M, Vignaud A, Ciuciu  
431 P. 2020. 3D variable[U+2010]density SPARKLING trajectories for high[U+2010]resolution  
432 T2\*[U+2010]weighted magnetic resonance imaging. *NMR in Biomedicine* 33. doi:10.1002/nbm.  
433 4349.
- 434 Lazarus C, Weiss P, Vignaud A, Ciuciu P. 2018. An empirical study of the maximum degree  
435 of undersampling in compressed sensing for T2\* -weighted MRI. *Magnetic Resonance Imaging*  
436 53:112–122. doi:10.1016/j.mri.2018.07.006.
- 437 Mccarthy JV, Mccarthy JV, Cotter TG. 2015. Cell shrinkage and apoptosis : a role for potassium  
438 and sodium ion efflux Cell shrinkage and apoptosis : a role for potassium and sodium ion efflux.  
439 *Cell Death and Differentiation* (1997) i:756–770.
- 440 Mir R, Guesalaga A, Spiniak J, Guarini M, Irarrazaval P. 2004. Fast three-dimensionalk-space  
441 trajectory design using missile guidance ideas. *Magnetic Resonance in Medicine* 52:329–336.  
442 doi:10.1002/mrm.20163.
- 443 Nagel AM, Laun FB, Weber MA, Matthies C, Semmler W, Schad LR. 2009. Sodium MRI using a  
444 density-adapted 3D radial acquisition technique. *Magnetic Resonance in Medicine* 62:1565–1573.  
445 doi:10.1002/mrm.22157.

- 446 Pipe JG, Menon P. 1999. Sampling density compensation in MRI: Rationale and an iterative numer-  
447 ical solution. *Magnetic Resonance in Medicine* 41:179–186. doi:10.1002/(SICI)1522-2594(199901)  
448 41:1<179::AID-MRM25>3.0.CO;2-V.
- 449 Porciuncula Baptista R, Vignaud A, Chaithya G R, Daval-Fr erot G, Mauconduit F, Naudin M,  
450 Lapert M, Guillevan R, Ciuciu P, Lerman-Rabrait C, Boumezbeur F. 2022. Evaluation of 3D  
451 SPARKLING for undersampled Sodium UTE MRI at ultra-high magnetic field. In: *Proceedings*  
452 *of the 30th International Society of Magnetic Resonance in Medicine*.
- 453 Reetz K, Romanzetti S, Dogan I, Sa  C, Werner CJ, Schiefer J, Schulz JB, Shah NJ. 2012. Increased  
454 brain tissue sodium concentration in Huntington’s Disease - A sodium imaging study at 4T.  
455 *NeuroImage* 63:517–524. doi:10.1016/j.neuroimage.2012.07.009.
- 456 Ridley B, Nagel AM, Bydder M, Maarouf A, Stellmann JP, Gherib S, Verneuil J, Viout P, Guye  
457 M, Ranjeva JP, Zaaraoui W. 2018. Distribution of brain sodium long and short relaxation times  
458 and concentrations: a multi-echo ultra-high field  $^{23}\text{Na}$  MRI study. *Scientific Reports* 8:1–12.  
459 doi:10.1038/s41598-018-22711-0.
- 460 Robison RK, Anderson AG, Pipe JG. 2017. Three-dimensional ultrashort echo-time imaging using  
461 a FLORET trajectory. *Magnetic Resonance in Medicine* 78:1038–1049. doi:10.1002/mrm.26500.
- 462 Romanzetti S, Mirkes CC, Fiege DP, Celik A, Felder J, Shah NJ. 2014. Mapping tissue sodium  
463 concentration in the human brain: A comparison of MR sequences at 9.4 Tesla. *NeuroImage*  
464 96:44–53. doi:10.1016/j.neuroimage.2014.03.079.
- 465 Stollberger R, Wach; P. 1995. Imaging of the active B1 field in vivo. *Magnetic Resonance in*  
466 *Medicine* :73–75doi:0740-3194/96.
- 467 Vasanaawala SS, Alley MT, Hargreaves Ba, Barth Ra, Pauly JM, Lustig M. 2010. Improved Pediatric  
468 MR Imaging with Compressed Sensing. *Radiology* 256:607–616. doi:10.1148/radiol.10091218.
- 469 Wang H, Hristov D, Qin J, Tian L, Willmann, J rgeren K. 2015. Three-dimensional Dynamic  
470 Contrast-enhanced US Imaging for Early Antiangiogenic. *Radiology* 277:424–434.
- 471 Zaaraoui W, Konstandin S, Audoin B, Nagel AM, Rico A, Malikova I, Soulier E, Viout P, Confort-  
472 Gouny S, Cozzone PJ, Pelletier J, Schad LR, Ranjeva JP. 2012. Distribution of Brain Sodium  
473 Accumulation Correlates with Disability in Multiple Sclerosis : A cross-sectional  $^{23}\text{Na}$  MR Imag-  
474 ing Study. *Radiology* 264:859–867. doi:10.1148/radiol.12112680/-/DC1.

475 Zanic O, Juras V, Szomolanyi P, Schreiner M, Raudner M, Giraudo C, Trattnig S. 2021. Frontiers of  
 476 sodium mri revisited: From cartilage to brain imaging. Journal of Magnetic Resonance Imaging  
 477 54:58–75.

## 478 Figures and Tables

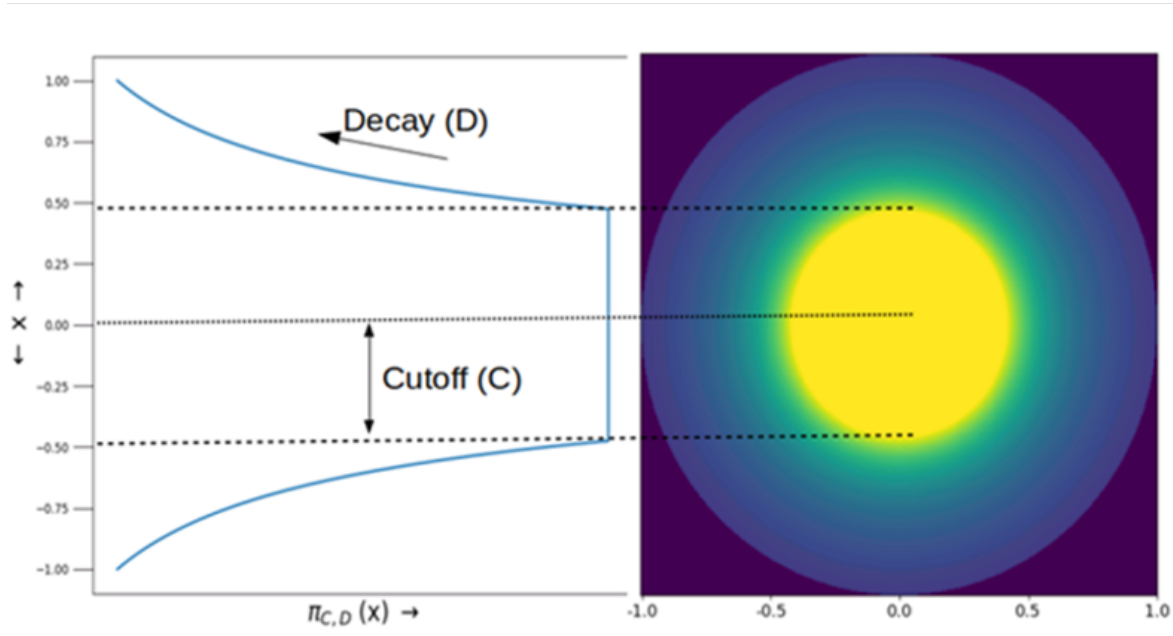


Figure 1: Target density function for SPARKLING and its parameters

Example of target density function for SPARKLING  $Pi_{C,D}(x)$  illustrating the definition of both parameters: cutt-off (C) and decay (D).

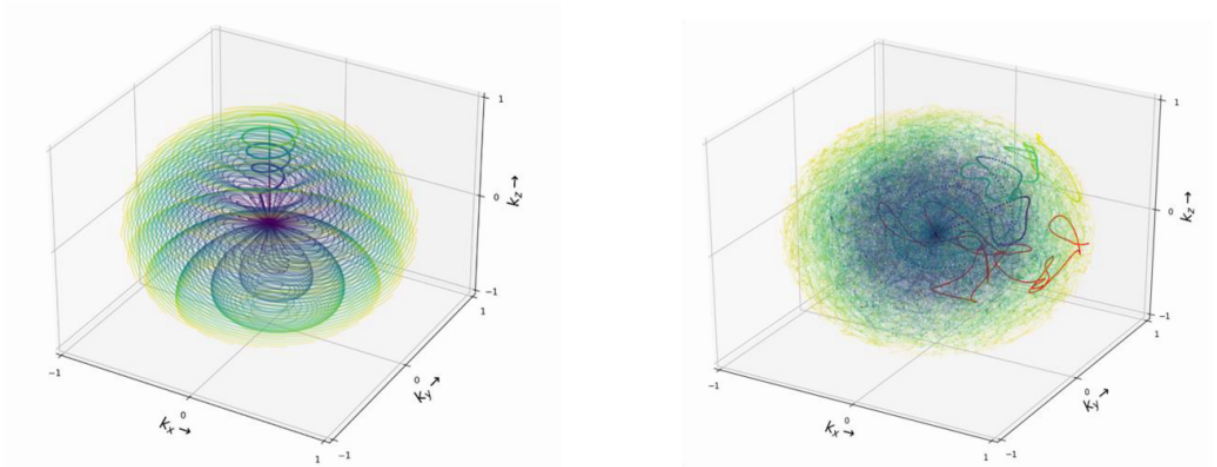


Figure 2: **TPI (left) and SPARKLING (right) k-space sampling schemes**

Each spoke is colored in blue at its start and in yellow at its end. For both TPI and SPARKLING,  $T_{obs}$  was equal to 12.48 ms.

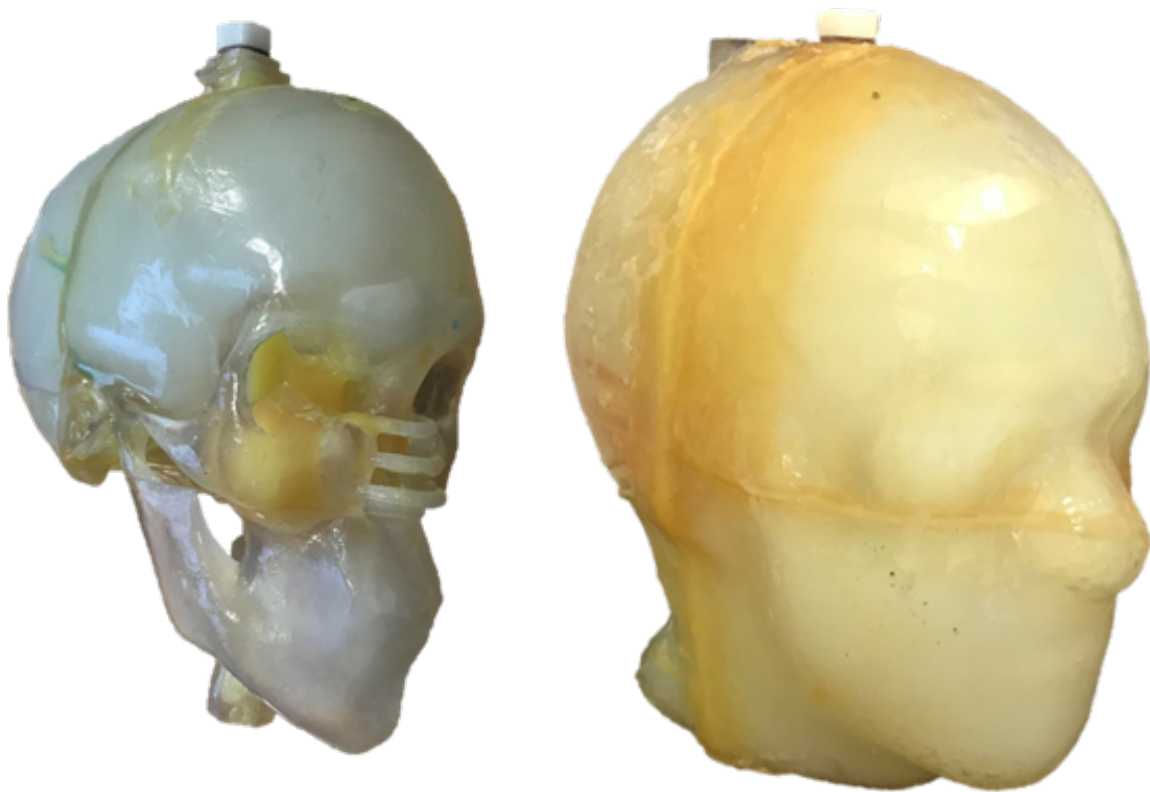


Figure 3: **Anthropomorphic human head phantom.**

The inner and outer compartments were filled respectively with a 40 and 100 mmol/L NaCl solution.

Courtesy of Thadee Delaree

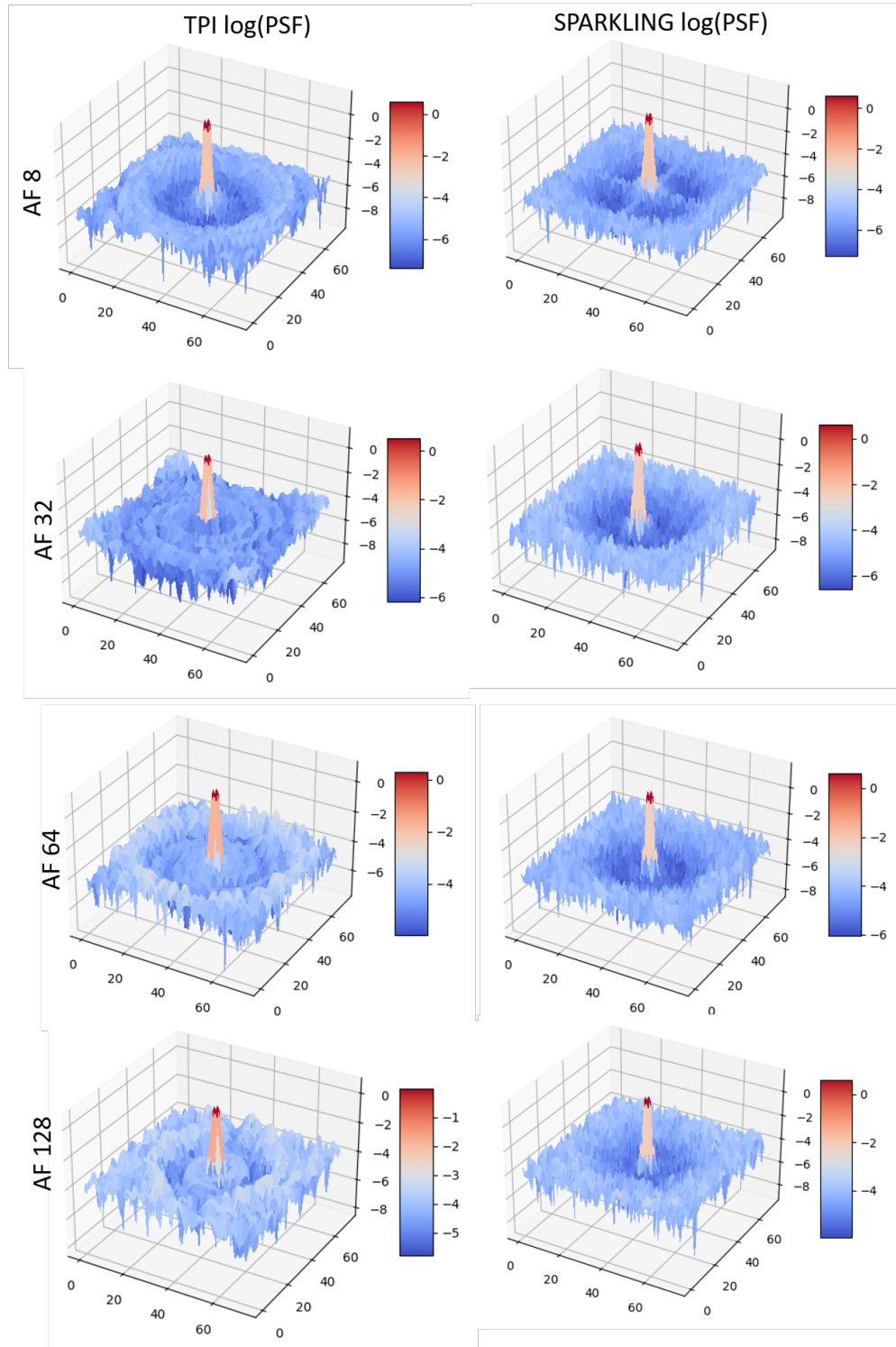


Figure 4: **Estimated Point-spread functions of each investigated undersampled SPARKLING and TPI k-space sampling strategy.**

The PSF are plotted in log scale to better visualize the ripples surrounding the central lobe.

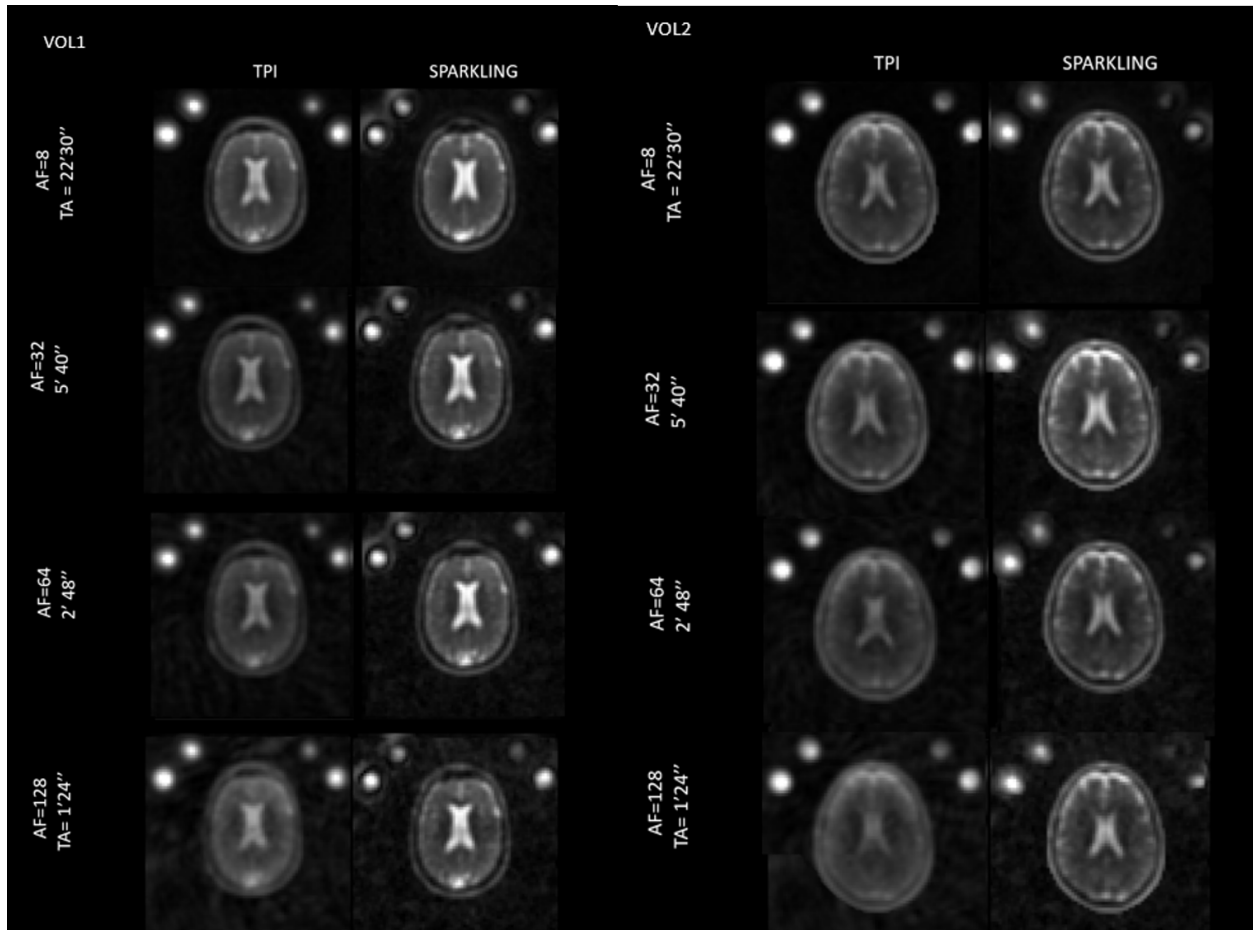


Figure 5: Undersampled TPI and SPARKLING acquisitions reconstructed with NUFFT with density compensation.

Isotropic resolution of 4 mm. TE/TR=0.8/20 ms. Acquisitions times indicated next to each image.

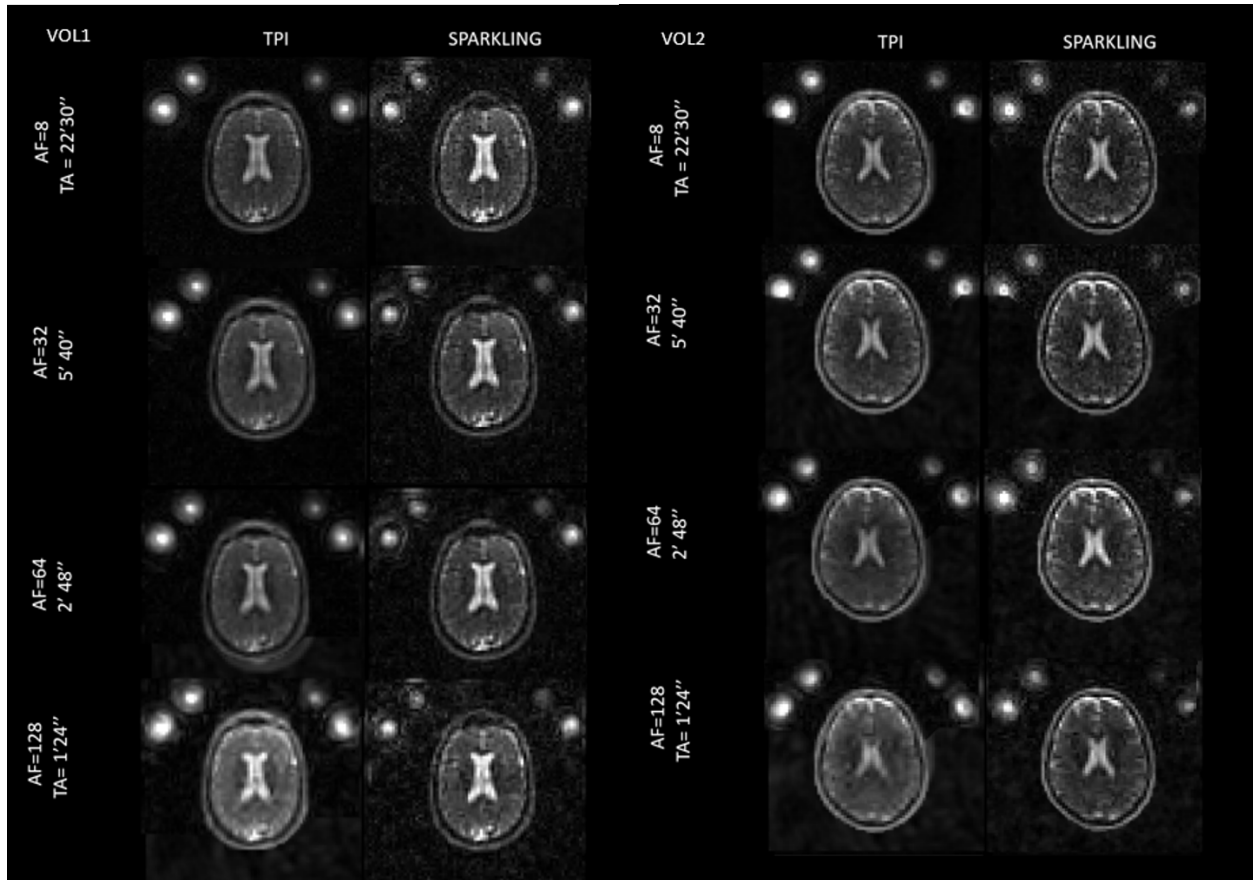


Figure 6: Undersampled TPI and SPARKLING acquisitions reconstructed with POGM iterative algorithm with density compensation.

Isotropic resolution of 4 mm. TE/TR=0.8/20 ms. Acquisitions times indicated next to each image.

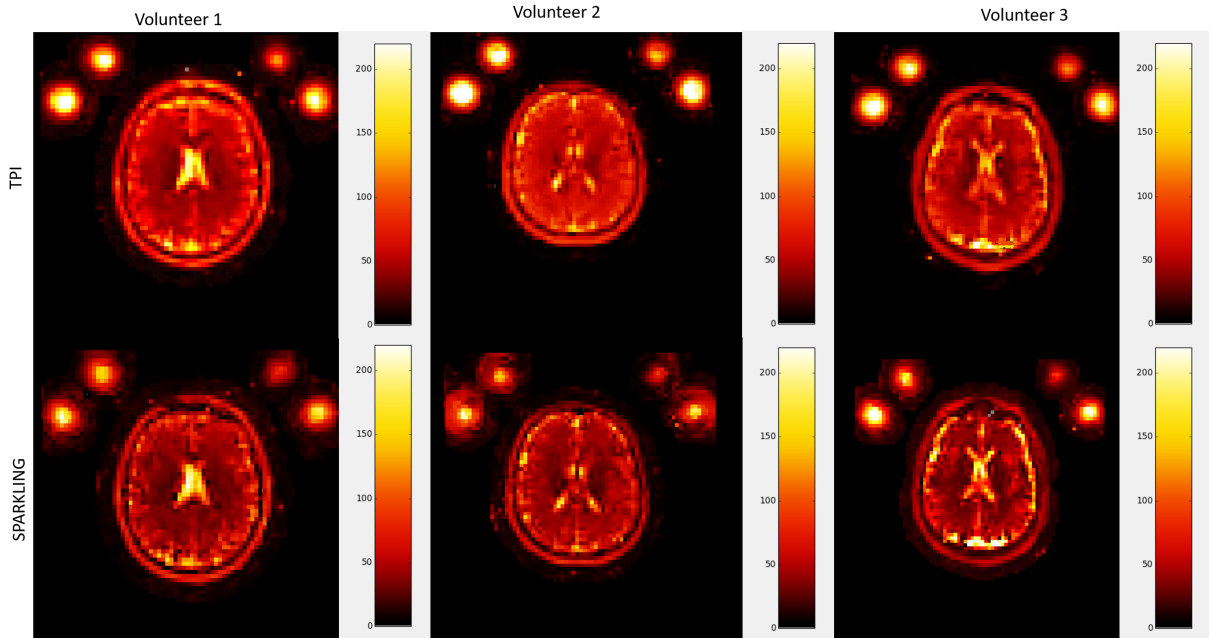


Figure 7: Comparison of the TSC maps obtained using undersampled TPI and SPARKLING acquisitions (AF=32) and POGM iterative reconstruction.

Isotropic resolution of 4 mm. TE/TR=0.8/20 ms. TA=11' 20 ".FA<sub>1</sub>/FA<sub>2</sub>=25/50.

Table 1: Full-width at half maximum (FWHM) for the Point-spread functions (PSF) estimated for each undersampling strategy.

Targeted spatial resolution (pixel size) is 4mm isotropic

	FWHM (in pixels in the three dimensions)			
	AF=8	AF=32	AF=64	AF=128
TPI	(2.4,2.4,2.4)	(2.6,2.6,2.6)	(2.6,2.6,2.6)	(2.6,2.6,2.6)
SPARKLING	(2.2,2.2,2.2)	(2.2,2.2,2.2)	(2.4,2.4,2.4)	(2.4,2.4,2.4)

Table 2: Mean TSC estimated within the inner compartment of the anthropomorphic phantom using NUFFT and increasing AF.

mean  $\pm$  standard deviation, concentrations expressed in mM. Expected TSC is 40 mM.

Trajectory \ AF	8	32	64	128
TPI	40 $\pm$ 4	42 $\pm$ 2	56 $\pm$ 4	74 $\pm$ 5
SPARKLING	42 $\pm$ 3	41 $\pm$ 2	55 $\pm$ 3	67 $\pm$ 4

Table 3: Mean TSC estimated within the inner compartment of the anthropomorphic phantom using POGM and increasing AF.

mean  $\pm$  standard deviation, concentrations expressed in mM. . Expected TSC is 40 mM.

Trajectory \ AF	8	32	64	128
TPI	42 $\pm$ 2	51 $\pm$ 3	70 $\pm$ 5	110 $\pm$ 7
SPARKLING	44 $\pm$ 2	39 $\pm$ 2	65 $\pm$ 5	103 $\pm$ 6

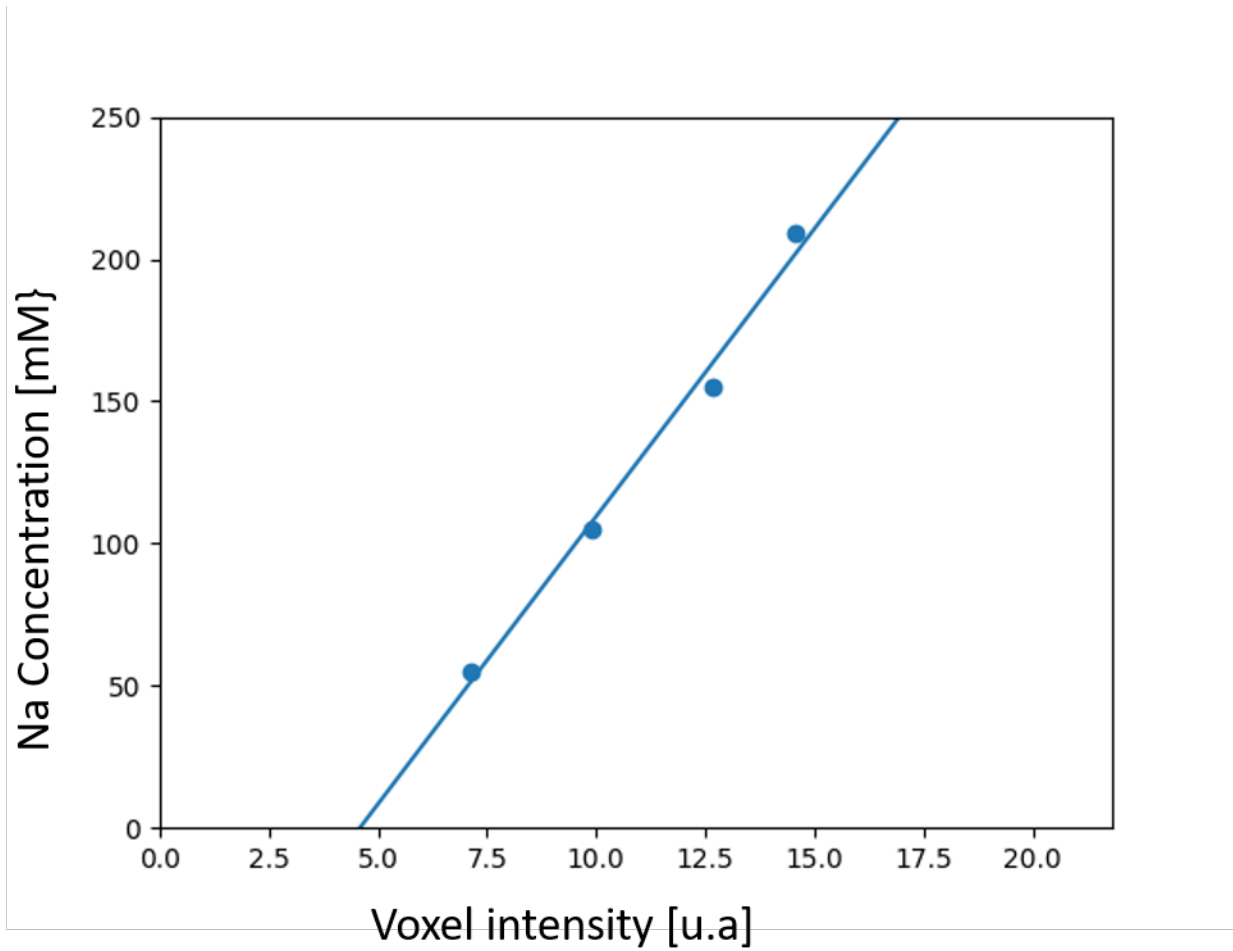


Figure S1: **Example of a 4-point calibration curve for one of the *in vitro* undersampled SPARKLING (AF=128) acquisition.**

The linear regression ( $R^2=0.99$ ) does not cross at (0,0) due to the background noise with a non-zero mean due to its Rician nature.